ACS Energy LETTERS

http://pubs.acs.org/journal/aelccp

Letter

Chemical Imaging of Cathode–Electrolyte Interphase in Sulfide Solid-State Batteries

Published as part of ACS Energy Letters special issue "The Evolving Landscape of Energy Research: Insights from Leading Researchers".

Lihong Zhao,[§] Qiuyi Yuan,*[,§] Wen Ren, Toshihiro Asada, Chaoshan Wu, Takanori Itoh, Suusaku Ogiu, Takashi Sanada, Shohei Yamashita, Daisuke Shibata, and Yan Yao*

Cite This: https://doi.org/10.1021/acsenergylett.5c03034

Read Online

ACCESS | Metrics & More | Article Recommendations | Supporting Information

ABSTRACT: The cathode–electrolyte interphase critically impacts the performance of solid-state batteries, yet its chemical evolution remains poorly understood, especially in sulfide systems. Here, we employ scanning transmission X-ray microscopy (STXM) to directly map the NMC–argyrodite interphase. We show that sulfide oxidation primarily occurs at the electrolyte surrounding the NMC particles, while the bulk electrolyte remains electrochemically stable. This interfacial oxidation, accompanied by Ni reduction, leads to the formation of P_2S_x, S^0, and SO_x^{2-} species at interphase. Our results provide direct evidence of cathode–electrolyte interactions and elucidate interfacial degradation.

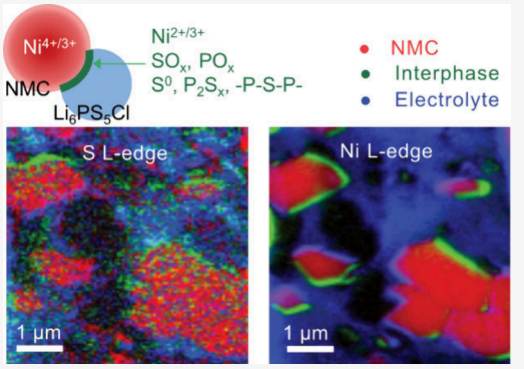

All-solid-state batteries (ASSBs) offer enhanced safety and the potential for higher energy density.[1−3] A composite cathode, typically comprised of active material, solid electrolyte, and conductive carbon, plays a pivotal role in determining cell energy density and rate capability.[4−7] To achieve optimal performance, the solid electrolyte within the cathode should exhibit high ionic conductivity to compensate for its tortuous structure, low mass density to reduce the weight fraction of inactive components, and good contact with the cathode to minimize interfacial resistance.[1,8] Sulfide electrolytes stand out as promising candidates for ASSBs due to their high Li-ion conductivity, moderate mass density, and excellent processability, which facilitate good interfacial contact.[9,10] However, sulfides are often plagued by interfacial side reactions, especially at high electrochemical potentials.[11] Understanding these reactions and the distribution of reaction products is critical to improve the overall battery performance.

Extensive studies have characterized interfacial side reactions between sulfide electrolytes and oxide cathodes. It is well established that sulfide (S^{2-}) undergoes oxidation to elemental sulfur (S^0) at high potentials.[11−13] Sulfur can then further oxidize into sulfites and sulfates in the presence of oxide cathodes during charging.[14] The resulting cathode–electrolyte interphase (CEI) hinders ion transport between the active material and the electrolyte, leading to increased impedance and overpotential during cycling.

Despite the critical role of the CEI in composite cathodes, little progress has been made in clarifying its origin—specifically, whether it arises solely from high electrochemical potential or from coupled chemical and electrochemical reactions. A major challenge lies in accurately probing redox species at the interface and in the adjacent electrolyte and layered oxide cathodes. Conventional techniques such as X-ray photoelectron spectroscopy (XPS) offer only limited insights as they measure oxidation states averaged over relatively large beam spots. Furthermore, layered oxide particles show interparticle and intraparticle heterogeneity in state-of-charge (SoC),[15−17] making bulk chemical measurements better suited to capturing overall reaction trends than to pinpointing the precise chemical processes at the interphase.

Other high-resolution methods also face limitations. Electron beam-based techniques such as scanning electron microscopy (SEM) and transmission electron microscopy (TEM) provide elemental information but lack sensitivity to chemical valence states.[18] Although electron energy-loss

Received: September 21, 2025
Revised: January 22, 2026
Accepted: February 10, 2026

spectroscopy provides information on chemical states, sulfide electrolytes are highly susceptible to beam damage in TEM, restricting most observations to residual electrolyte near active materials, even with lamella samples.[19] Optical spectroscopy methods generally lack the spatial resolution required to probe nanoscale interfacial features.[20] Time-of-flight secondary ion mass spectrometry (ToF-SIMS) can detect fragments of interfacial side products and visualize CEI around active material particles,[21−23] but it cannot definitively resolve their chemical states. The comparison of characterization techniques for solid-state batteries is summarized in Table S1.

Scanning X-ray imaging has emerged as a promising technique for mapping the evolution of chemical states in battery systems with high spatial resolution.[24−26] It has been used to track lithiation states in individual cathode particles[15,16,27,28] and to probe degradation at cathode−electrolyte interfaces in semisolid[29,30] and solid polymer batteries.[31] However, due to challenges in sample preparation and the limited availability of soft X-ray sources, scanning transmission X-ray microscopy (STXM) has not yet been widely applied to sulfide-based solid electrolytes.

In this work, we employ STXM to visualize the chemical state evolution in composite cathodes of sulfide-based ASSBs. We provide direct evidence of sulfide oxidation and nickel reduction at the cathode−electrolyte interphase, validating mechanisms previously inferred from indirect characterization. By mapping the oxidation state of sulfur within the composite cathode, we reveal that high electrochemical potential alone is insufficient to degrade sulfide electrolytes; instead, degradation is strongly facilitated by the presence of cathode active materials.

NMC-Argyrodite Degradation at High Cutoff Voltage

STXM was used to directly visualize the chemical states of both the cathode and electrolyte components at the nanoscale. Figure 1 schematically illustrates the imaging procedure and data collection process. The composite cathode was thinned into an ∼100 nm lamella and transferred to the STXM chamber under Ar protection. At each scan step, X-ray transmission was acquired and singular value decomposition (SVD) was applied to segment images based on spectral variations, enabling chemical mapping of the imaged region. We used single-crystal NMC ($LiNi_{0.83}Mn_{0.06}Co_{0.11}O_2$) and argyrodite ($Li_6PS_5Cl$) as a model system to study CEI formation.

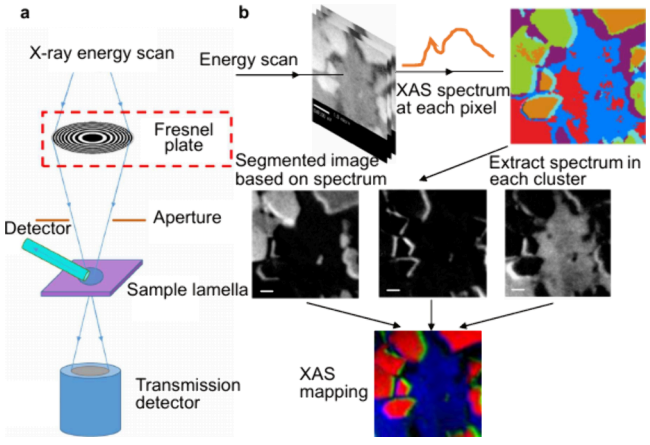

Figure 1. Chemical mapping of composite cathodes. (a) Schematic illustration of the STXM measurement; (b) flowchart of the characterization procedure. The composite cathode was prepared into a lamella using FIB-SEM, followed by XAS spectrum acquisition at each pixel. The resulting images were segmented based on spectral features using SVD to generate the XAS map.

To study the CEI formation, the composite cathode was intentionally subjected to harsh cycling. As a baseline, cells were cycled between 2.6−4.25 V vs Li^+/Li. Voltage profiles (Figure 2a) and capacity retention curves (Figure 2c) showed reasonable performance: a reversible capacity at 218 mAh/g at 0.1 C, an initial Coulombic efficiency (ICE) of 84%, and 93% capacity retention after 100 cycles at 2C.

Increasing the cutoff to 4.7 V vs Li^+/Li (Figure 2b) boosted the first-cycle discharge capacity to 239 mAh/g with ICE of 81%, but capacity faded rapidly, retaining only 77% after 100 cycles (Figure 2d). Cycling at 4.7 V also induced a stronger voltage hysteresis (Figure 2e). At 4.25 V cutoff, the average discharge potential was 0.2 V lower than the average charge potential; at 4.7 V, this difference expanded from 0.6 to 1.0 V over 100 cycles, indicating progressive interfacial impedance. Differential capacity (dQ/dV) analysis (Figure 2f) provides further insight into the degradation mechanism. During the initial charge, extending the cutoff voltage to 4.7 V does not introduce additional redox peaks in the high-voltage region compared with the 4.25 V cutoff sample, suggesting the absence of new bulk redox processes. However, the corresponding discharge profile exhibits a shift of the H2/H3 peak toward a lower potential, indicating that the initial high-voltage charge already induces irreversible impedance that hinders the H2/H3 redox reaction. After 100 cycles, the dQ/dV peaks show significant attenuation, particularly for the 4.7 V-cycled cell, likely suggesting decreased electrochemical accessibility of active NMC particles. Consistent with the electrochemical profile, the cross-section imaging after cycling at 4.7 V (Figure S1) revealed cracks within NMC and partial loss of contact at the NMC−SE interface.

Electrochemical impedance spectra collected at 4.25 V vs Li^+/Li after the 5th, 25th, 50th, and 100th cycle (Figure 2g) reinforced these findings. The impedance of cells cycled to 4.25 V cutoff remained nearly unchanged, whereas those cycled to 4.7 V exhibited rapid growth. Interfacial resistance (R_{int}) increased linearly with the square root of cycle number, consistent with the classical solid−electrolyte interphase (SEI) growth model, which suggests the evolution of an electronically insulating but ionically conductive interphase.[32,33] The impedance spectra are further analyzed with the distribution of relaxation time (DRT) method to separate contributions from processes occurring at different length scales.[34] Figure 2h,i shows that impedance associated with short characteristic times, which represents Li transport across the chemical interphase, increases only modestly during cycling. In contrast, the dominant impedance growth at higher cutoff voltage likely arises from midfrequency features associated with larger-length-scale processes, such as mechanical cracking and interfacial delamination.

Shift in Ni and S Oxidation State at the Interface

The chemical state evolution of NMC and argyrodite was investigated by using X-ray absorption spectroscopy (XAS) in different detection modes (Figure 3a). Total electron yield (TEY) probes the surface (∼10 nm), partial fluorescence yield (PFY) and inverse partial fluorescence yield (IPFY) capture subsurface signals (∼hundreds of nm), while STXM detects

https://doi.org/10.1021/acsenergylett.5c03034
ACS Energy Lett. XXXX, XXX, XXX−XXX

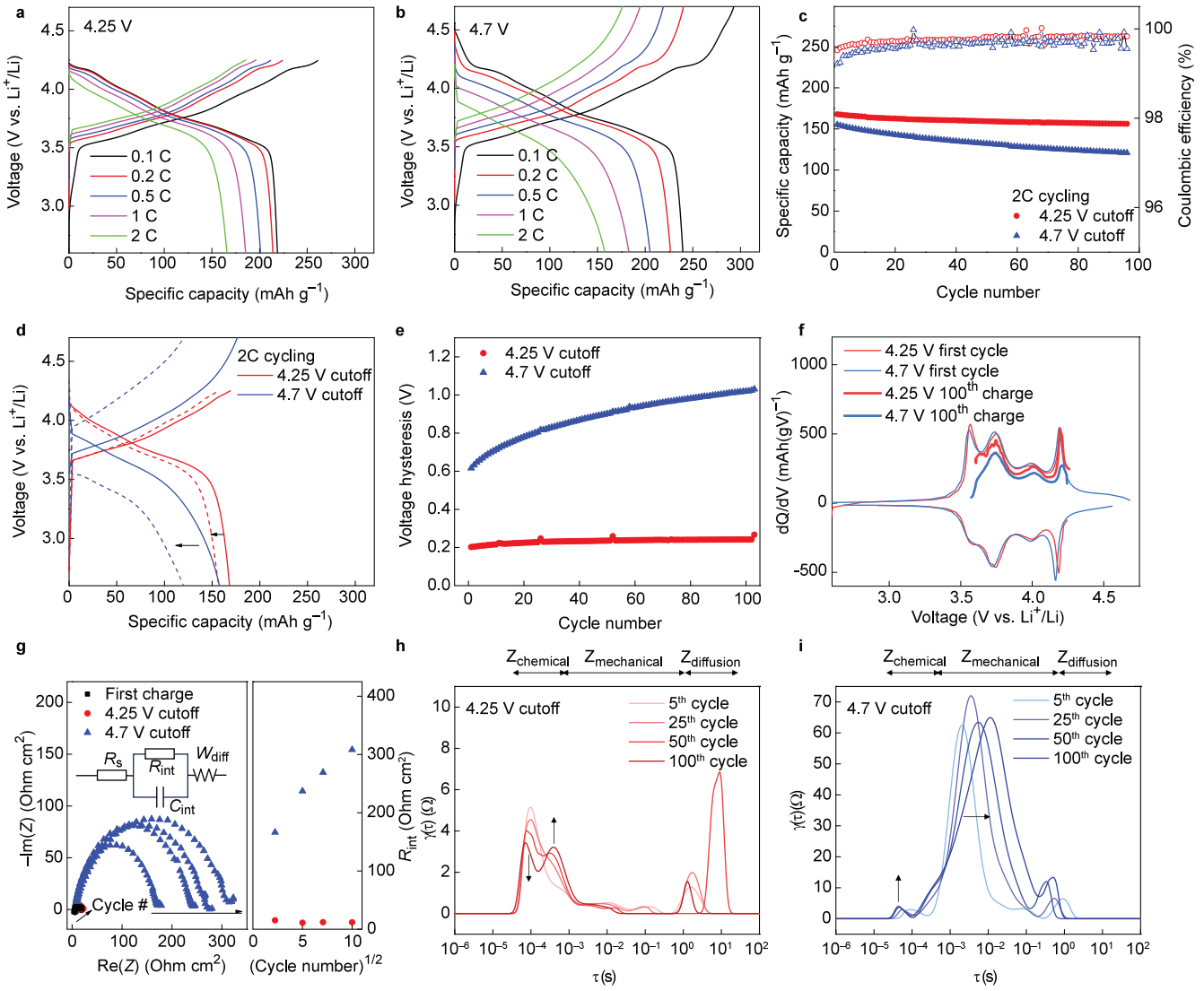

Figure 2. Electrochemical performance of the NMC-argyrodite cathode at different cutoff voltages. (a) Voltage profile at 4.25 V cutoff; (b) voltage profile at 4.7 V cutoff; (c) capacity retention over 100 cycles at 2C; (d) capacity and voltage decay from the 1st to 100th cycle at 2C; (e) voltage hysteresis over 100 cycles at 2C; (f) differential capacity profile of the first cycle and the last charge at 0.1 C. (g) Electrochemical impedance at 5th, 25th, 50th, and 100th cycles, measured at fully charged state. The inset shows the equivalent circuit model. The charge-transfer resistance increases linearly with the square root of the cycle number. DRT analysis of impedance evolution during cycling. (h) 4.25 V cutoff; (i) 4.7 V cutoff.

bulk transmission.[15] Here, we employed NiL-edge IPFY to eliminate the self-absorption effect inherent to PFY owing to its high concentration.[35]

XAS spectra were compared for three conditions: the pristine sample (2.6 V vs Li^+/Li), the charged sample (first charged to 4.25 V vs Li^+/Li), and the cycled sample (100 cycles at 4.25 V, followed by charging to 4.25 V vs Li^+/Li). In Ni IPFY spectra (Figure 3b), two peaks at 850 and 852 eV correspond to t_{2g} and e_g states, respectively. A higher e_g/t_{2g} ratio indicates a higher oxidation state.[36] For the charged samples, the e_g/t_{2g} ratio was ~6.8, significantly higher than the value of ~1.0 in the pristine state (Figure 3f). A similar trend appeared in Ni TEY spectra (Figure 3e), although with lower ratios of 1.6 (charged) and 0.7 (pristine), suggesting that the NMC surface is more reduced than the bulk. The difference in Ni oxidation state between IPFY and TEY observed in the pristine sample can be attributed to the instability of surface Ni, especially for Ni-rich NMCs.[37] In contrast, the difference between surface and subsurface Ni in charged samples is more significant than that in pristine samples, which is likely driven by interfacial interactions with the sulfide electrolyte.

O K-edge PFY spectra (Figure 3c) exhibited a pre-edge feature at 528 eV, corresponding to hybridization between transition metal 3d and oxygen 2p orbitals, along with main-edge features above 535 eV.[38] A minor peak at 532.5 eV is attributed to surface Li_2CO_3.[37] A larger pre-edge peak area correlated with higher transition metal oxidation states, consistent with the Ni L-edge results showing Ni oxidation upon charging.

In S L-edge TEY spectra, both the charge state and cycling history significantly influence spectral features. In the pristine state, two peaks at 161.5 and 162.8 eV are consistent with S^{2-}. Upon charging, regardless of cycling history, these peaks shifted to 162.0 and 163.3 eV, reflecting decreased electron density around sulfur and indicating oxidation of S^{2-} to S^0.[39] Additional peaks at ~172 eV correspond to SO_x^{2-} species.[40]

Together, these measurements establish a baseline for STXM analysis. Bulk spectroscopy reveals that surface sulfur

https://doi.org/10.1021/acsenergylett.5c03034
ACS Energy Lett. XXXX, XXX, XXX−XXX

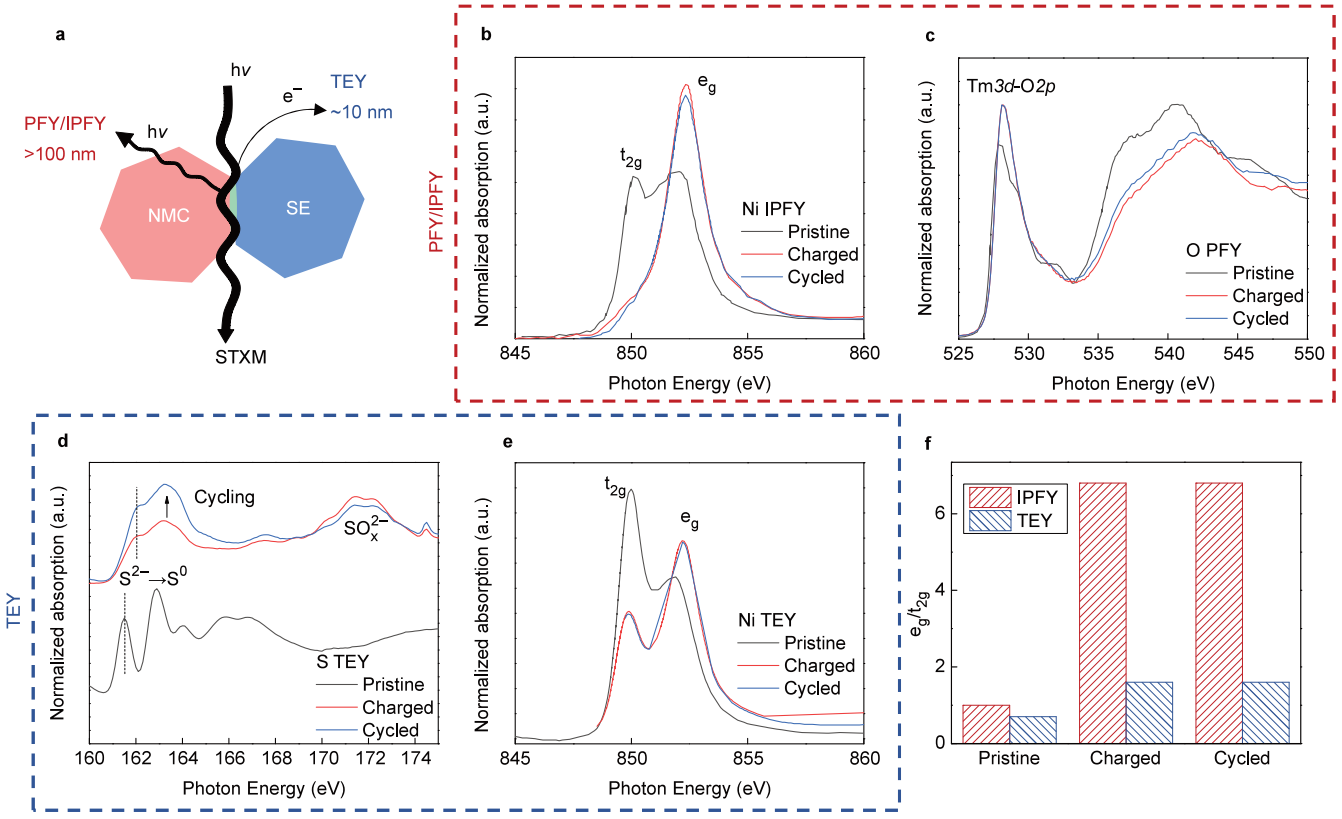

Figure 3. X-ray absorption spectra of composite cathodes. (a) Schematic illustration of the probing depth of PFY/IPFY, TEY, and STXM measurements; (b) Ni IPFY spectra; (c) O PFY spectra; (d) S TEY spectra; (e) Ni TEY spectra; (f) e_g/t_{2g} ratio of Ni. The pristine sample (black) corresponds to the NMC-argyrodite composite cathode at 2.6 V vs Li^+/Li. The charged sample (red) represents the cathode charged to 4.25 V vs Li^+/Li during the first charge. The cycled sample (blue) represents the cathode after 100 cycles between 2.6–4.25 V vs Li^+/Li, followed by a final charge to 4.25 V vs Li^+/Li.

oxidizes to S^0 and SO_x^{2-} upon charging, with little dependence on cycling. On the cathode side, Ni shows a lower oxidation state at the surface (~10 nm) compared to the subsurface (~hundreds of nanometers), likely due to interfacial side reactions between NMC and the sulfide electrolyte.

Chemical Imaging of Cathode–Electrolyte Interphase

To simultaneously observe the solid electrolyte and active material, S and Ni L-edges were selected for STXM characterization. Figure 4 shows the evolution of the chemical state at the electrode level. Three conditions were compared at the charged state (4.25 V vs Li^+/Li): without prior cycling (Figure 4a–d), after 100 cycles at 4.25 V cutoff (Figure 4e–h), and after 100 cycles at 4.7 V cutoff (Figure 4i–l). In SEM images (Figure 4a,e,i), smooth, dense regions correspond to a single-crystalline NMC, while porous regions represent the solid electrolyte. Although all three lamellae show similar morphology, the sample cycled to 4.7 V displays large transverse cracks (Figure S1), likely caused by the reversible volume change of NMC (~5%) and irreversible electrolyte expansion driven by chemical and electrochemical side reactions.[41,42] We also compared the STXM images of the first and the last scan and observed no visible change in morphology or contrast (Figure S2), indicating relatively minor beam damage during the measurement.

Interfacial reactions are revealed by the S L-edge mapping. In the bulk electrolyte (blue), the S L-edge consistently shows a low-energy peak at around 163.9 eV across all samples, characteristic of S^{2-} in argyrodite. Despite the relatively low signal-to-noise ratio due to the limited photon flux of the beamline at this energy range, these spectra closely resemble the TEY spectrum of pristine electrolyte, indicating minimal side reactions within bulk electrolyte particles. At the interphase (green) between the NMC and electrolyte, however, the S L-edge shifts to higher energy (164.1 eV) after cycling. This shift is statistically significant based on Gaussian fitting of the edge jump (Figure S3) and is consistent with oxidation of sulfide species toward S^0. No statistically significant differences were observed among interphase spectra obtained under different cycling histories (4.25 V vs 4.7 V), indicating that variations in interphase chemical composition are relatively minor within the resolution and sensitivity of the present STXM measurements. Despite the presence of conductive carbon in the composite cathode, no electrolyte oxidation was observed in the bulk, suggesting that sulfide degradation is unlikely to occur solely due to the high potential. Instead, active materials, such as NMC, are required to drive interfacial sulfide oxidation.

The O K-edge XAS spectra show clear differences between pristine and charged NMC, reflecting the expected evolution of the oxygen electronic structure upon delithiation (Figure 3c). However, no discernible difference is observed between the single-charged sample and the sample after 100 cycles at the same SoC. This indicates that the O K-edge evolution is primarily governed by the SoC rather than cycling history. Consistently, no additional O K-edge shifts were detected in STXM measurements acquired at identical states of charge (Figure S4). These results suggest that while oxidative species

https://doi.org/10.1021/acsenergylett.5c03034
ACS Energy Lett. XXXX, XXX, XXX–XXX

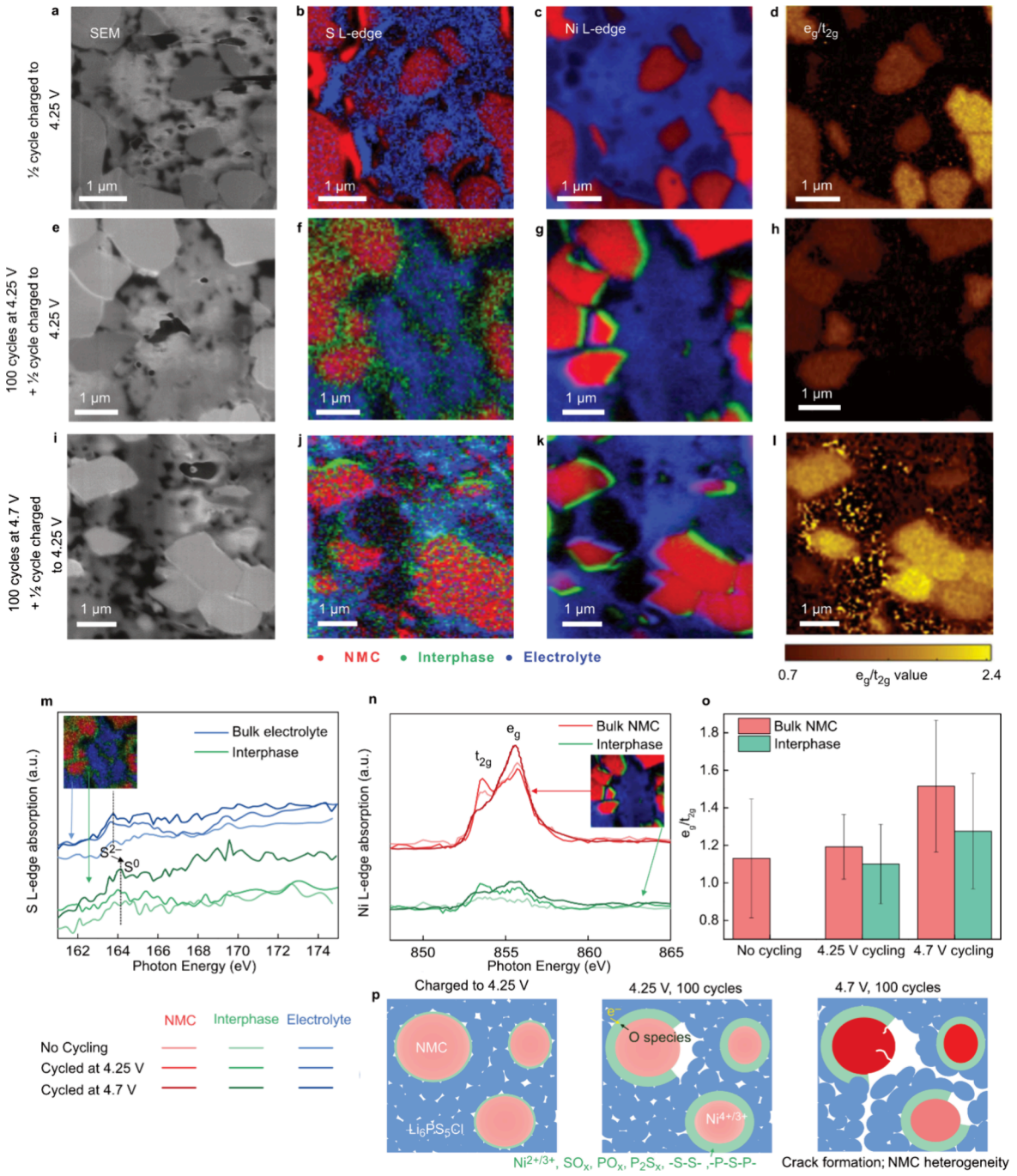

Figure 4. XAS mapping of the NMC−argyrodite interface. (a−d) SEM, S L-edge, Ni L-edge, and Ni e_g/t_{2g} mapping of an NMC-Li_6PS_5Cl laminate charged to 4.25 V vs Li^+/Li without cycling; (e−h) corresponding maps of a laminate charged to 4.25 V after 100 cycles at 4.25 V; (i−l) corresponding maps of a laminate at charged state 4.25 V after 100 cycles at 4.7 V. Red, green, and blue regions correspond to NMC, the interphase, and the electrolyte, respectively. (m) S L-edge and (n) Ni L-edge spectra collected from bulk NMC (red), interphase (green), and bulk electrolyte (blue) region; inset indicates the representative sampling locations. Line colors with varying lightness correspond to different samples, as shown at the bottom right of the panel. (o) Ni e_g/t_{2g} ratio extracted from bulk NMC (red) and interphase (green) regions; error bars represent standard deviation across particles. (p) Schematic illustration of the interfacial reaction between NMC and argyrodite. The difference in color saturation within NMC particles represents heterogeneity in Ni oxidation state after prolonged cycling at high cutoff voltage. NMC surface in contact with electrolyte exhibits lower valence.

may form transiently at the NMC surface at high voltage, they likely react rapidly with the sulfide electrolyte to form an interphase, thereby suppressing detectable oxygen signatures in both bulk and spatially resolved measurements.

The interphase thickness evolves with cycling. After a single charge to 4.25 V, only a negligible interphase was detected, with a thickness below the STXM spatial resolution (50 nm), as no distinct region could be resolved by SVD fitting. After 100 cycles, however, the interfacial region (green) expanded significantly (Figure 4f,j). Statistical analysis based on Ni L-edge spectra revealed no substantial difference in the average interphase thickness between the 4.25 V-cycled cell (93 ± 43

https://doi.org/10.1021/acsenergylett.5c03034
ACS Energy Lett. XXXX, XXX, XXX−XXX

nm) and the 4.7 V-cycled cell (89 ± 66 nm) (Figure S5). In addition, S L-edge spectra indicated no obvious change in the chemical state between these two samples. Combining this observation with DRT analysis, these results suggest that the pronounced voltage hysteresis and impedance increase observed at higher cutoff voltages primarily originate from electrode cracking and interfacial delamination rather than from interphase thickening or composition change, which appear to play a relatively minor role.

Alongside sulfur oxidation, Ni reduction at the interphase is evident. The e_g/t_{2g} ratio is consistently lower at the interphase (green) than that in bulk NMC (red) (Figure 4n,o). After one charge to 4.25 V, no interfacial Ni reduction was observed (Figure 4c). After 100 cycles, however, the interphase thickens for both cutoff voltages (Figure 4g,k), accompanied by a significant decrease in the Ni valence localized at the NMC-argyrodite interphase. Spatial mapping of the Ni e_g/t_{2g} ratio (Figure 4h,l) highlights a darker contrast at NMC surfaces adjacent to the electrolyte compared to bulk NMC, reflecting localized reduction.

To quantitatively validate the correlation between Ni valence and contact with the electrolyte, we compared the e_g/t_{2g} ratio at NMC surfaces in direct contact with the electrolyte to that at NMC surfaces adjacent to macroscopic voids in the composite cathode. Figure S6 compares statistical distributions of the e_g/t_{2g} ratio at different locations, including bulk NMC, at the interphase in contact with electrolyte, and at the interphase in contact with voids. In bulk NMC, 100 cycles at a 4.25 V cutoff slightly increased the average NMC oxidation state (Figure S6a,b). In contrast, increasing the cutoff voltage to 4.7 V results in a bimodal distribution of Ni oxidation states (Figure S6c), indicating increased heterogeneity in Ni valence across particles even though all samples were charged to the same state of charge prior to characterization. This behavior is likely associated with degraded Li transport kinetics within the composite cathode following high-voltage cycling, which limits Li reintercalation during the final charge.[26]

In the interphase region, the e_g/t_{2g} ratio at NMC surfaces in contact with the electrolyte (Figure S6g,h) is statistically significantly lower than that at NMC surfaces adjacent to voids but not in contact with the electrolyte (Figure S6e,f), with a two-tailed p value less than 0.01. The result further demonstrates that contact with the sulfide electrolyte is the origin of the reduced Ni valence at the NMC surface.

Interestingly, individual NMC particles show different states of charge, reflecting particle-level heterogeneity in the composite cathode. Such heterogeneity arises from uneven access to ionic and electronic transport pathways due to the complex cathode microstructure.[26] The e_g/t_{2g} ratio for each NMC particle is plotted in Figure S7, where each data point represents an individual particle and the error bar represents the standard deviation of e_g/t_{2g} ratio within the particle. While the intraparticle variation in e_g/t_{2g} is relatively small, a much larger deviation is observed in the interparticle statistics. No statistically significant correlation is found between Ni valence and particle size (Figure S7a) or between Ni valence and the perimeter contact ratio with the electrolyte (Figure S7b). Nevertheless, the e_g/t_{2g} ratio of NMC cycled at 4.7 V exhibits a broader distribution, consistent with our prior observation of increased heterogeneity in Figure S6.

Overall, chemical mapping directly supports the proposed cathode degradation mechanism (Figure 4p). Repeated cycling, especially at high cutoff voltages, leads to sulfide oxidation at the NMC surface, while the bulk electrolyte remains stable despite accessibility to electrons at high potential due to the uniform distribution of conductive carbon (Figure S8). Although the exact nature of the oxygen-containing species and their release mechanism from NMC remain under debate, an oxidative NMC surface likely accelerates electrolyte oxidation near active particles.[43,44] Concurrently, interfacial Ni reduction occurs, producing an increasingly thick interphase. Over time, this process increases impedance and voltage hysteresis, ultimately limiting electrochemical performance.

Interfacial chemical reactions were further confirmed by XPS of the composite cathodes at the charged state. Compared to STXM, XPS involves significantly less beam-induced damage and therefore provides a complementary and more reliable approach to cross-validate the interfacial chemistry inferred from STXM and bulk XAS. After 100 cycles at 4.25 and 4.7 V, the S 2p peak for argyrodite (161.7 eV) reduced from 42% to 33% and 13%, respectively, while the S^0 content (164.4 eV) increased from 12% to 17% and 28% (Figure 5a–c, Table S2).

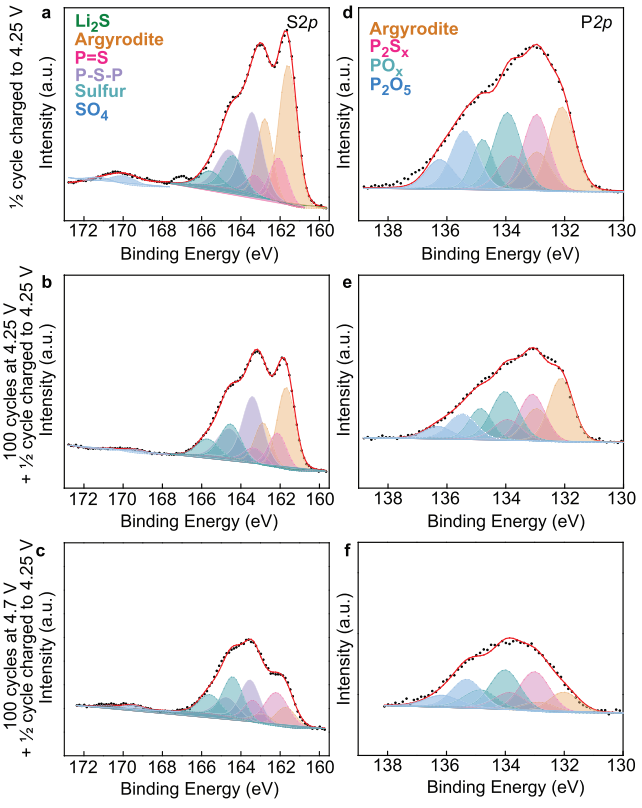

Figure 5. XPS spectra of NMC–argyrodite interphase. (a–c) sulfur 2p spectra at charged state (4.25 V vs Li^+/Li) with no extra cycling (a), 100 cycles at 4.25 V (b), and 100 cycles at 4.7 V (c), respectively; (d–f) phosphorus 2p spectra at charged state (4.25 V vs Li^+/Li) with no extra cycling (d), 100 cycles at 4.25 V (e), and 100 cycles at 4.7 V (f), respectively.

The contribution of SO_4^{2-} (169.2 eV) remained consistently low (2–3%). These results align with XAS and STXM (Figures 3 and 4), confirming S^0 as the primary side product. The weak SO_x signal appears to be intrinsic to the sample, as evidenced by XPS results, despite of the possible reduction induced by X-ray during STXM measurements. A similar trend appeared in P 2p spectra: argyrodite (132.0 eV) decreased from 33% to 16%,

https://doi.org/10.1021/acsenergylett.5c03034
ACS Energy Lett. XXXX, XXX, XXX–XXX

while P_2S_x (133.0 eV) and PO_x (134.0 eV) slightly increased after cycling (Figure 5d–f, Table S3).

To verify the role of NMC in driving electrolyte oxidation, we further performed XPS on a control composite consisting of Li_6PS_5Cl mixed with conductive carbon but without NMC. The composite was electrochemically oxidized by holding the cell at 4.25 and 4.7 V (Figure S9), thereby excluding chemical oxidation by the oxide cathode. XPS spectra were then collected by using the same acquisition and fitting procedures (Figure S10). In the absence of NMC, electrochemically oxidized Li_6PS_5Cl exhibits relatively simple decomposition products, with argyrodite, P–S–P, elemental sulfur, and minor Li_2S impurities detected in the S 2p spectra. Consistent behavior is observed in the P 2p spectra, where only the argyrodite and P_2S_x peaks are present, with no evidence of the PO_x and P_2O_5 species. In contrast, Li_6PS_5Cl oxidized within composite cathodes containing NMC shows substantially broadened and more complex S 2p and P 2p features, suggesting multiple intermediate oxidation species, as well as higher-valence sulfur and phosphorus species.

Taken together, the convergence of particle-resolved STXM mapping, bulk-averaged XAS and XPS, and electrochemical analyses provides a coherent and internally consistent picture of interfacial degradation, ensuring that our conclusions do not rely on a single localized measurement.

In summary, we directly visualized interfacial degradation in NMC-argyrodite composite cathodes for solid-state batteries by using STXM chemical mapping. Together with other spectroscopy methods, factors like CEI formation, NMC inhomogeneity, contact loss caused by morphology change, and their contributions to cell performance degradation under various cell conditions, including cycle number and cutoff voltage, were evaluated. High-voltage cycling accelerates sulfide oxidation, especially at the NMC interface, forming P_2S_x, S^0, and SO_x^{2-} while the bulk electrolyte remains stable. Concurrently, interfacial Ni reduction occurs. Progressive interphase growth and electrode cracking raise the impedance, leading to capacity fading and voltage hysteresis. This work provides clear evidence of cathode–electrolyte reactions and offers a direct visualization of interfacial degradation. STXM, by integration with both morphological and chemical information, is a powerful tool for elucidating degradation mechanisms in solid-state batteries.

EXPERIMENTAL METHODS

Materials and Electrode Fabrication

Single-crystal $LiNi_{0.83}Mn_{0.06}Co_{0.11}O_2$ (NMC, MSE Supplies) was used as the cathode active material, Li_6PS_5Cl (LPSCl, MSE Supplies) was used in the solid electrolyte and in the composite cathode, vapor-grown carbon fibers (VGCF) (PR-19-XT-HHT, Applied Sciences) were used as a conductive additive, and PTFE (Sigma) was used as a binder for composite cathode fabrication. PTFE binder is mandatory to maintain the mechanical integrity of the FIB-cut cathode lamella. Li–Mg foil (90 μm, MSE Supplies) was used as the anode, with nearly identical electrode potential compared to Li (1 mV vs Li^+/Li) while providing better stability at high current densities. NMC, LPSCl, VGCF, and PTFE were mixed in a mass ratio of 70:27:3:0.5 in a hot mortar and pestle to fibrilize the binder. The mixture was further rolled with a metal rod on a hot plate to achieve the desired thickness and finally tailored to an 11.1 mm free-standing disk.

Electrochemical Characterization of Full Cells

Electrochemical tests were carried out in polyether–ether–ketone (PEEK) die cells with a diameter of 12.7 mm. Typically, 130 mg of solid electrolyte powder was compressed in the die under 150 MPa to form a pellet. A composite cathode disk (8.89 mg active material, 1.4 mAh cm^{-2}) was placed on one side of the solid electrolyte and further densified at 375 MPa. After densification, a piece of ~90 μm Li–Mg foil was added to the counter side and further pressed at 50 MPa for 1 min to improve interfacial contact. The cell is subject to a stack pressure of 14 MPa. All evaluations were done at a temperature of 60 °C within a climate-controlled oven using a VMP-3 potentiostat. Electrochemical impedance spectra were collected from 1 MHz to 100 mHz at 7 mV amplitude. For samples at the charged state, the cell was charged to 4.25 V vs Li^+/Li at 0.1 C. For the cycled cathode, the cell was cycled at a 2C rate with 4.25 and 4.7 V cutoff voltages for 100 cycles, then charged to 4.25 V at 0.1 C to maintain consistency in sample state-of-charge. Pellet cells were removed from the PEEK die and cut into 3 pieces using a ceramic cutter for STXM, XAS, and XPS characterizations.

STXM Characterization

To allow the X-ray to be able to transmit at the S L- and Ni L-edge, the pellet cells were cut into 100 nm-thick lamella with an area of 7 × 7 μm^2 using cryogenic plasma-FIB (Helios G4 PFIB Cxe, Thermo Scientific) under the acceleration voltage of 30 keV. The pellet surface was gently scratched with a ceramic razor blade before preparation. The sampling area was determined by observing the surface EDX and finding an area that included both NMC and SE particles. To avoid any FIB-introduced damage to the lamella, we used cryogenic conditions at −150 °C and a Xe plasma beam. The STXM experiment was conducted at BL-19A, Photon Factory, KEK (Figure S11). The beamline was optimized for energy around 500–1000 eV to cover the Ni L- and O K-edge. Incident X-ray radiation was focused through a Fresnel zone plate. aXis2000 was used for STXM data processing and SVD analysis.[45] All transfer and characterization, including PFIB, were carried out under Ar protection.

Image Analysis

Image processing was performed by referencing SEM images to separate particles and interphase components from the original images; regions outside the analysis area were masked such that their pixel values were set to zero. The Ni oxidation state histogram was constructed by dividing the intensity range into ten bins based on the range between 0.7 and 2.4 shown in Figure 4d,h,l while excluding zero. Each bin was mapped to an 8-bit scale (256 levels). Masking was conducted using image-editing software Adobe Photoshop, and calculations of layer thickness and histogram were conducted using Python 3.14.

XAS Characterization

S L- and Ni L-edge PFY/IPFY and TEY spectra were collected from the top surface of the composite cathode at BL-11, SR center, Ritsumeikan University, with a grating as a monochromator. The sample surface was gently scratched with a ceramic razor blade to avoid potential surface contamination. A transfer vessel was used to protect the samples from air during transportation. All spectra were processed using Athena for background removal and normalization.[46]

XPS Characterization

All samples were transferred to XPS (VersaProbeIII, ULVAC-PHI) using a transfer vessel to protect the samples from air. Similar to XAS, the sample surface was scratched with a ceramic razor blade. XPS was measured using a monochromized Al Kα source (1486.6 eV), with a beam size of Φ200 μm. Spectra scans were taken under the condition of 50 W power, 45° takeoff angle, and pass energy of 69 eV. Peak fitting was carried out using MultiPak using Shirley for background removal.

ASSOCIATED CONTENT

Supporting Information

The Supporting Information is available free of charge at https://pubs.acs.org/doi/10.1021/acsenergylett.5c03034.

https://doi.org/10.1021/acsenergylett.5c03034
ACS Energy Lett. XXXX, XXX, XXX–XXX

Detailed XPS analysis, post-mortem SEM of composite cathode, O K-edge XAS, statistical analysis of STXM mapping, XPS of electrochemically oxidized argyrodite, and experimental setup (PDF)

AUTHOR INFORMATION

Corresponding Authors

Qiuyi Yuan − *Nissan ARC LTD., Yokosuka, Kanagawa 2370061, Japan;* orcid.org/0000-0001-9274-8558; Email: q-yuan@nissan-arc.co.jp

Yan Yao − *Department of Electrical and Computer Engineering, and Texas Center for Superconductivity at the University of Houston, University of Houston, Texas 77204, United States; Energy Storage Research Alliance, Argonne National Laboratory, Lemont, Illinois 60439, United States;* orcid.org/0000-0002-8785-5030; Email: yyao4@uh.edu

Authors

Lihong Zhao − *Department of Electrical and Computer Engineering, and Texas Center for Superconductivity at the University of Houston, University of Houston, Texas 77204, United States;* orcid.org/0000-0003-2308-1053

Wen Ren − *Department of Chemical and Biomolecular Engineering, University of Houston, Texas 77204, United States;* orcid.org/0000-0002-1461-6717

Toshihiro Asada − *Nissan ARC LTD., Yokosuka, Kanagawa 2370061, Japan*

Chaoshan Wu − *Department of Electrical and Computer Engineering, and Texas Center for Superconductivity at the University of Houston, University of Houston, Texas 77204, United States;* orcid.org/0000-0003-3458-8300

Takanori Itoh − *Nissan ARC LTD., Yokosuka, Kanagawa 2370061, Japan*

Suusaku Ogiu − *Nissan ARC LTD., Yokosuka, Kanagawa 2370061, Japan*

Takashi Sanada − *Nissan ARC LTD., Yokosuka, Kanagawa 2370061, Japan*

Shohei Yamashita − *IMSS, KEK, Tsukuba, Ibaraki 3050801, Japan*

Daisuke Shibata − *SR center, Research Organization of Science and Technology, Ritsumeikan University, Kusatsu City, Shiga 5258577, Japan*

Complete contact information is available at: https://pubs.acs.org/10.1021/acsenergylett.5c03034

Author Contributions

[§]L.Z. and Q.Y contributed equally to this work.

Notes

The authors declare the following competing financial interest(s): Y.Y. has equity interest in LiBeyond, LLC and Solid Design Instruments, LLC. The University of Houston reviewed and approved his relationship in compliance with its conflict-of-interest policy. The remaining authors declare no competing interests.

ACKNOWLEDGMENTS

This work is funded by the Energy Storage Research Alliance "ESRA" (DE-AC02-06CH11357), an Energy Innovation Hub funded by the U.S. Department of Energy, Office of Science, Basic Energy Sciences. STXM experiment was carried out under the approval of PAC No. 2021G592 and XAS was under Proposal No. S22011 of Ritsumeikan SR center.

REFERENCES

(1) Janek, J.; Zeier, W. G. Challenges in Speeding up Solid-State Battery Development. *Nat. Energy* **2023**, *8* (3), 230−240.

(2) Zhao, L.; Lakraychi, A. E.; Chen, Z.; Liang, Y.; Yao, Y. Roadmap of Solid-State Lithium-Organic Batteries toward 500 Wh kg^{-1}. *ACS Energy Lett.* **2021**, *6* (9), 3287−3306.

(3) Guo, L.; Zheng, J.; Zhao, L.; Yao, Y. Interfacial Instabilities in Halide-Based Solid-State Batteries. *MRS Bull.* **2023**, *48* (12), 1247−1256.

(4) Zhang, J.; Chen, Z.; Ai, Q.; Terlier, T.; Hao, F.; Liang, Y.; Guo, H.; Lou, J.; Yao, Y. Microstructure Engineering of Solid-State Composite Cathode via Solvent-Assisted Processing. *Joule* **2021**, *5*, 1845−1859.

(5) Le, M.; Yao, A.; Zhang, A.; Le, H.; Chen, Z.; Wu, X.; Zhao, L.; Chen, J. Expediting Ionic Conductivity Prediction of Solid-State Battery Electrodes Using Machine Learning. *IEEE J. Multiscale Multiphysics Comput. Technol.* **2024**, *9*, 375−382.

(6) Hao, F.; Liang, Y.; Zhang, Y.; Chen, Z.; Zhang, J.; Ai, Q.; Guo, H.; Fan, Z.; Lou, J.; Yao, Y. High-Energy All-Solid-State Organic−Lithium Batteries Based on Ceramic Electrolytes. *ACS Energy Lett.* **2021**, *6* (1), 201−207.

(7) Hao, F.; Chi, X.; Liang, Y.; Zhang, Y.; Xu, R.; Guo, H.; Terlier, T.; Dong, H.; Zhao, K.; Lou, J.; Yao, Y. Taming Active Material-Solid Electrolyte Interfaces with Organic Cathode for All-Solid-State Batteries. *Joule* **2019**, *3* (5), 1349−1359.

(8) Shi, T.; Tu, Q.; Tian, Y.; Xiao, Y.; Miara, L. J.; Kononova, O.; Ceder, G. High Active Material Loading in All-Solid-State Battery Electrode via Particle Size Optimization. *Adv. Energy Mater.* **2020**, *10* (1), 1902881.

(9) Wu, C.; Lou, J.; Zhang, J.; Chen, Z.; Kakar, A.; Emley, B.; Ai, Q.; Guo, H.; Liang, Y.; Lou, J.; Yao, Y.; Fan, Z. Current Status and Future Directions of All-Solid-State Batteries with Lithium Metal Anodes, Sulfide Electrolytes, and Layered Ternary Oxide Cathodes. *Nano Energy* **2021**, *87*, 106081.

(10) Tan, D. H. S.; Meng, Y. S.; Jang, J. Scaling up High-Energy-Density Sulfidic Solid-State Batteries: A Lab-to-Pilot Perspective. *Joule* **2022**, *6* (8), 1755−1769.

(11) Schwietert, T. K.; Arszelewska, V. A.; Wang, C.; Yu, C.; Vasileiadis, A.; Klerk, N. J. J. de; Hageman, J.; Hupfer, T.; Kerkamm, I.; Xu, Y.; Maas, E. van der; Kelder, E. M.; Ganapathy, S.; Wagemaker, M. Clarifying the Relationship between Redox Activity and Electrochemical Stability in Solid Electrolytes. *Nat. Mater.* **2020**, *19* (4), 428−435.

(12) Minnmann, P.; Quillman, L.; Burkhardt, S.; Richter, F. H.; Janek, J. Editors' Choice—Quantifying the Impact of Charge Transport Bottlenecks in Composite Cathodes of All-Solid-State Batteries. *J. Electrochem. Soc.* **2021**, *168* (4), 040537.

(13) Jung, S.-K.; Gwon, H.; Lee, S.-S.; Kim, H.; Lee, J. C.; Chung, J. G.; Park, S. Y.; Aihara, Y.; Im, D. Understanding the Effects of Chemical Reactions at the Cathode−Electrolyte Interface in Sulfide Based All-Solid-State Batteries. *J. Mater. Chem. A* **2019**, *7* (40), 22967−22976.

(14) Walther, F.; Koerver, R.; Fuchs, T.; Ohno, S.; Sann, J.; Rohnke, M.; Zeier, W. G.; Janek, J. Visualization of the Interfacial Decomposition of Composite Cathodes in Argyrodite-Based All-Solid-State Batteries Using Time-of-Flight Secondary-Ion Mass Spectrometry. *Chem. Mater.* **2019**, *31* (10), 3745−3755.

(15) Gent, W. E.; Lim, K.; Liang, Y.; Li, Q.; Barnes, T.; Ahn, S.-J.; Stone, K. H.; McIntire, M.; Hong, J.; Song, J. H.; Li, Y.; Mehta, A.; Ermon, S.; Tyliszczak, T.; Kilcoyne, D.; Vine, D.; Park, J.-H.; Doo, S.-K.; Toney, M. F.; Yang, W.; Prendergast, D.; Chueh, W. C. Coupling between Oxygen Redox and Cation Migration Explains Unusual Electrochemistry in Lithium-Rich Layered Oxides. *Nat. Commun.* **2017**, *8* (1), 2091.

(16) Park, J.; Zhao, H.; Kang, S. D.; Lim, K.; Chen, C.-C.; Yu, Y.-S.; Braatz, R. D.; Shapiro, D. A.; Hong, J.; Toney, M. F.; Bazant, M. Z.;

Chueh, W. C. Fictitious Phase Separation in Li Layered Oxides Driven by Electro-Autocatalysis. *Nat. Mater.* **2021**, *20* (7), 991−999.
(17) Yang, Z.; Lin, F. Heterogeneous, Defect-Rich Battery Particles and Electrodes: Why Do They Matter, and How Can One Leverage Them? *J. Phys. Chem. C* **2021**, *125* (18), 9618−9629.
(18) Liu, G.; Lu, Y.; Wan, H.; Weng, W.; Cai, L.; Li, Z.; Que, X.; Liu, H.; Yao, X. Passivation of the Cathode−Electrolyte Interface for 5 V-Class All-Solid-State Batteries. *ACS Appl. Mater. Interfaces* **2020**, *12* (25), 28083−28090.
(19) Zhang, R.; Strauss, F.; Jiang, L.; Casalena, L.; Li, L.; Janek, J.; Kondrakov, A.; Brezesinski, T. Transition-Metal Interdiffusion and Solid Electrolyte Poisoning in All-Solid-State Batteries Revealed by Cryo-TEM. *Chem. Commun.* **2023**, *59* (31), 4600−4603.
(20) Lou, S.; Yu, Z.; Liu, Q.; Wang, H.; Chen, M.; Wang, J. Multi-Scale Imaging of Solid-State Battery Interfaces: From Atomic Scale to Macroscopic Scale. *Chem.* **2020**, *6* (9), 2199−2218.
(21) Ai, Q.; Chen, Z.; Zhang, B.; Wang, F.; Zhai, T.; Liu, Y.; Zhu, Y.; Terlier, T.; Fang, Q.; Liang, Y.; Zhao, L.; Wu, C.; Guo, H.; Fan, Z.; Tang, M.; Yao, Y.; Lou, J. High-Spatial-Resolution Quantitative Chemomechanical Mapping of Organic Composite Cathodes for Sulfide-Based Solid-State Batteries. *ACS Energy Lett.* **2023**, *8* (2), 1107−1113.
(22) Zuo, T.; Walther, F.; Teo, J. H.; Rueß, R.; Wang, Y.; Rohnke, M.; Schröder, D.; Nazar, L. F.; Janek, J. Impact of the Chlorination of Lithium Argyrodites on the Electrolyte/Cathode Interface in Solid-State Batteries. *Angew. Chem., Int. Ed.* **2023**, *62* (7), No. e202213228.
(23) Walther, F.; Randau, S.; Schneider, Y.; Sann, J.; Rohnke, M.; Richter, F. H.; Zeier, W. G.; Janek, J. Influence of Carbon Additives on the Decomposition Pathways in Cathodes of Lithium Thiophosphate-Based All-Solid-State Batteries. *Chem. Mater.* **2020**, *32* (14), 6123−6136.
(24) Temprano, I.; Carrasco, J.; Bugnet, M.; Lucas, I. T.; Zhou, J.; Weatherup, R. S.; O'Keefe, C. A.; Ruff, Z.; Xu, J.; Folastre, N.; Wang, J.; Gajan, A.; Demortière, A. Advanced Methods for Characterizing Battery Interfaces: Towards a Comprehensive Understanding of Interfacial Evolution in Modern Batteries. *Energy Storage Mater.* **2024**, *73*, 103794.
(25) Kim, J.; Lee, D.; Nam, C.; Chung, J.; Koo, B.; Kim, N.; Lim, J. Energy Material Analysis via In-Situ/Operando Scanning Transmission X-Ray Microscopy: A Review. *J. Electron Spectrosc. Relat. Phenom.* **2023**, *266*, 147337.
(26) Lim, J.; Li, Y.; Alsem, D. H.; So, H.; Lee, S. C.; Bai, P.; Cogswell, D. A.; Liu, X.; Jin, N.; Yu, Y.; Salmon, N. J.; Shapiro, D. A.; Bazant, M. Z.; Tyliszczak, T.; Chueh, W. C. Origin and Hysteresis of Lithium Compositional Spatiodynamics within Battery Primary Particles. *Science* **2016**, *353* (6299), 566−571.
(27) Sun, T.; Sun, G.; Yu, F.; Mao, Y.; Tai, R.; Zhang, X.; Shao, G.; Wang, Z.; Wang, J.; Zhou, J. Soft X-ray Ptychography Chemical Imaging of Degradation in a Composite Surface-Reconstructed Li-Rich Cathode. *ACS Nano* **2021**, *15* (1), 1475−1485.
(28) Sun, G.; Wang, H.; Lee, C.; Zhu, Q.; Gao, L.; Hsieh, S.; Shao, Y.; Ishii, H.; Zhou, J.; Wang, J.; Wang, Z. Visualization of Thermal-Induced Degradation Pathways of High-Ni Cathode: A Comparative Study in Solid Chloride and Liquid Electrolytes. *Adv. Mater.* **2025**, *37*, No. e10392.
(29) Yan, S.; Abouali, S.; Yim, C.-H.; Zhou, J.; Wang, J.; Baranova, E. A.; Weck, A.; Thangadurai, V.; Merati, A.; Abu-Lebdeh, Y. Revealing the Role of Liquid Electrolytes in Cycling of Garnet-Based Solid-State Lithium-Metal Batteries. *J. Phys. Chem. C* **2022**, *126* (33), 14027−14035.
(30) Yan, S.; Yim, C.-H.; Zhou, J.; Wang, J.; Abouali, S.; Baranova, E. A.; Weck, A.; Thangadurai, V.; Merati, A.; Abu-Lebdeh, Y. Elucidating the Origins of Rapid Capacity Fade in Hybrid Garnet-Based Solid-State Lithium Metal Batteries. *J. Phys. Chem. C* **2023**, *127* (51), 24641−24650.
(31) Lou, S.; Liu, Q.; Zhang, F.; Liu, Q.; Yu, Z.; Mu, T.; Zhao, Y.; Borovilas, J.; Chen, Y.; Ge, M.; Xiao, X.; Lee, W.-K.; Yin, G.; Yang, Y.; Sun, X.; Wang, J. Insights into Interfacial Effect and Local Lithium-Ion Transport in Polycrystalline Cathodes of Solid-State Batteries. *Nat. Commun.* **2020**, *11* (1), 5700.
(32) Alt, C. D.; Müller, N. U. C. B.; Riegger, L. M.; Aktekin, B.; Minnmann, P.; Peppler, K.; Janek, J. Quantifying Multiphase SEI Growth in Sulfide Solid Electrolytes. *Joule* **2024**, *8* (10), 2755−2776.
(33) Zuo, T.-T.; Rueß, R.; Pan, R.; Walther, F.; Rohnke, M.; Hori, S.; Kanno, R.; Schröder, D.; Janek, J. A Mechanistic Investigation of the $Li_{10}GeP_2S_{12}|LiNi_{1-x-y}Co_xMn_yO_2$ Interface Stability in All-Solid-State Lithium Batteries. *Nat. Commun.* **2021**, *12* (1), 6669.
(34) Wan, T. H.; Saccoccio, M.; Chen, C.; Ciucci, F. Influence of the Discretization Methods on the Distribution of Relaxation Times Deconvolution: Implementing Radial Basis Functions with DRTtools. *Electrochim. Acta* **2015**, *184*, 483−499.
(35) Achkar, A. J.; Regier, T. Z.; Wadati, H.; Kim, Y.-J.; Zhang, H.; Hawthorn, D. G. Bulk Sensitive X-Ray Absorption Spectroscopy Free of Self-Absorption Effects. *Phys. Rev. B* **2011**, *83* (8), 081106.
(36) Banerjee, A.; Tang, H.; Wang, X.; Cheng, J.-H.; Nguyen, H.; Zhang, M.; Tan, D. H. S.; Wynn, T. A.; Wu, E. A.; Doux, J.-M.; Wu, T.; Ma, L.; Sterbinsky, G. E.; D'Souza, M. S.; Ong, S. P.; Meng, Y. S. Revealing Nanoscale Solid−Solid Interfacial Phenomena for Long-Life and High-Energy All-Solid-State Batteries. *ACS Appl. Mater. Interfaces* **2019**, *11* (46), 43138−43145.
(37) Tian, C.; Nordlund, D.; Xin, H. L.; Xu, Y.; Liu, Y.; Sokaras, D.; Lin, F.; Doeff, M. M. Depth-Dependent Redox Behavior of $LiNi_{0.6}Mn_{0.2}Co_{0.2}O_2$. *J. Electrochem. Soc.* **2018**, *165* (3), A696−A704.
(38) Ramesh, N.; Banerjee, H.; Swallow, J. E. N.; Björklund, E.; Dean, A.; Didwal, P.; Fraser, M.; Phelan, C. M. E.; An, L.; Singh, J.; Lewis, J.; Song, W.; House, R. A.; Morris, A. J.; Weatherup, R. S.; Nicholls, R. J. Atomistic Interpretation of the Oxygen K-Edge X-Ray Absorption Spectra of Layered Li-Ion Battery Cathode Materials. *Chem. Mater.* **2024**, *36* (22), 11051−11064.
(39) Fleet, M. E. XANES Spectroscopy of Sulfur in Earth Materials. *Can. Miner.* **2005**, *43* (6), 1811−1838.
(40) Gilbert, B.; Perfetti, L.; Fauchoux, O.; Redondo, J.; Baudat, P.-A.; Andres, R.; Neumann, M.; Steen, S.; Gabel, D.; Mercanti, D.; Ciotti, M. T.; Perfetti, P.; Margaritondo, G.; Stasio, G. D. Spectromicroscopy of Boron in Human Glioblastomas Following Administration of $Na_2B_{12}H_{11}SH$. *Phys. Rev. E* **2000**, *62* (1), 1110−1118.
(41) Komatsu, H.; Banerjee, S.; Chandrappa, M. L. H.; Qi, J.; Radhakrishnan, B.; Kuwata, S.; Sakamoto, K.; Ong, S. P. Interfacial Stability of Layered $LiNi_xMn_yCo_{1-x-y}O_2$ Cathodes with Sulfide Solid Electrolytes in All-Solid-State Rechargeable Lithium-Ion Batteries from First-Principles Calculations. *J. Phys. Chem. C* **2022**, *126* (41), 17482−17489.
(42) Farzanian, S.; Mercado, J. V.; Shozib, I.; Sivadas, N.; Lacivita, V.; Wang, Y.; Tu, Q. H. Mechanical Investigations of Composite Cathode Degradation in All-Solid-State Batteries. *ACS Appl. Energy Mater.* **2023**, *6* (18), 9615−9623.
(43) Jung, R.; Metzger, M.; Maglia, F.; Stinner, C.; Gasteiger, H. A. Oxygen Release and Its Effect on the Cycling Stability of $LiNi_xMn_yCo_zO_2$ (NMC) Cathode Materials for Li-Ion Batteries. *J. Electrochem. Soc.* **2017**, *164* (7), A1361−A1377.
(44) Gao, X.; Li, B.; Kummer, K.; Geondzhian, A.; Aksyonov, D. A.; Dedryvère, R.; Foix, D.; Rousse, G.; Yahia, M. B.; Doublet, M.-L.; Abakumov, A. M.; Tarascon, J.-M. Clarifying the Origin of Molecular O_2 in Cathode Oxides. *Nat. Mater.* **2025**, *24* (5), 743−752.
(45) Hitchcock, A. P. Analysis of X-Ray Images and Spectra (aXis2000): A Toolkit for the Analysis of X-Ray Spectromicroscopy Data. *J. Electron Spectrosc. Relat. Phenom.* **2023**, *266*, 147360.
(46) Ravel, B.; Newville, M. *ATHENA, ARTEMIS, HEPHAESTUS*: Data Analysis for X-Ray Absorption Spectroscopy Using IFEFFIT. *J. Synchrotron Radiat.* **2005**, *12* (4), 537−541.

https://doi.org/10.1021/acsenergylett.5c03034
ACS Energy Lett. XXXX, XXX, XXX−XXX